

## COMPACT OUTFLOWS ASSOCIATED WITH TMC-1 AND TMC-1A

C. J. CHANDLER

Mullard Radio Astronomy Observatory, Cavendish Laboratory, Madingley Road, Cambridge CB3 0HE, UK

S. TEREBEY

Infrared Processing and Analysis Center, Jet Propulsion Laboratory and California Institute of Technology, IPAC 100-22,  
Caltech, Pasadena, CA 91125M. BARSONY<sup>1</sup>

Physics Department, University of California, Riverside, CA 92521

T. J. T. MOORE

School of Electrical Engineering, Liverpool John Moores University, Byrom Street, Liverpool L3 3AF, UK

AND

T. N. GAUTIER

Jet Propulsion Laboratory, MS 169-327, 4800 Oak Grove Drive, Pasadena, CA 91109

*Received 1996 April 26; accepted 1996 June 3*

## ABSTRACT

High spatial resolution observations are presented of the compact outflows associated with the young protostars TMC-1 (IRAS 04381+2540) and TMC-1A (IRAS 04365+2535) in Taurus. Emission in CO(1–0) imaged with the Owens Valley Millimeter Array shows the outflow lobes to be conical close to the star. Analysis of the outflow dynamics indicates that these objects are low-luminosity versions of the energetic outflows more commonly observed. Near-infrared images at *H* and *K* bands show a close correspondence between reflection nebulosity and the location of high-velocity gas and suggest the outflow cavity is evacuated, as do position-velocity diagrams of the CO(2–1). Comparison of the *J* = 1–0 transition with emission in the 2–1 line indicates that the excitation temperature in the high-velocity gas is higher than the surrounding Taurus cloud. We place limits on the inclination of both objects by comparing the data with theoretical outflow models and conclude that  $i \sim 40^\circ$ – $70^\circ$  for both objects. The deprojected opening angles of the outflow cones are then in the range  $30^\circ$ – $40^\circ$ .

None of the current outflow models satisfactorily explains the results for TMC-1 and TMC-1A, which are among the youngest class I sources in Taurus. We find their outflow structure shares many similarities with the more obscured and possibly younger class 0 objects, B335 and L1448-C. The main difference is the lower mechanical luminosities of the TMC-1 and TMC-1A outflows, reflecting a factor of 3–4 smaller linear extent and velocity and a factor of 10–20 lower mass than the L1448-C molecular jet source. Taken together, the four protostars share the common properties of (1) conical outflow lobes close to the star, (2) evacuated outflow cavities, and (3) relatively wide  $30^\circ$ – $45^\circ$  opening angles. A successful theory of young stellar outflows must be able to explain these characteristics.

*Subject headings:* infrared: ISM: continuum — ISM: individual (TMC-1, TMC-1A) —  
ISM: jets and outflows — reflection nebulae — stars: formation

## 1. INTRODUCTION

All stars are thought to go through a phase of energetic mass loss during their formation most commonly observed as high-velocity molecular outflows. It is still not clear how the outflows are driven, nor how the molecular gas is accelerated, yet it is essential to understand outflows if star formation in general is to be understood.

A common outflow mechanism in both low- and high-mass sources is implied by the good correlations found between the bolometric source luminosity and outflow momentum flux and outflow mechanical luminosity for young stars (Bally & Lada 1983; Edwards, Ray, & Mundt 1993; Cabrit & Bertout 1992). If there is a common mechanism we might expect the physical and dynamical properties of outflows from low- and high-mass objects to be similar. Recent models for the driving of molecular outflows (e.g., Shu et al. 1991; Masson & Chernin 1992, 1993; Stahler 1994) have begun to make definite predictions for the observed structure of outflows, particularly close to the

exciting star. High spatial resolution observations of the outflows from nearby protostars, which are predominantly low-mass, therefore have the potential to distinguish between different models.

The strongest constraints on the driving and acceleration mechanisms of outflows are best obtained through observations of young, unevolved outflows, where the cloud core has not yet been significantly dispersed by the process of star formation. Statistical arguments indicate that outflows start when the central protostar is less than a few  $\times 10^4$  yr old (Parker, Padman, & Scott 1991), as does the recent study of VLA 1623 (André, Ward-Thompson, & Barsony 1993). We might therefore hope to find the youngest, least-evolved outflows from the protostars which have not yet accumulated much mass.

To try to distinguish between various models for the outflow driving mechanism and the acceleration of ambient gas, we have carried out a detailed, high-resolution study of two young embedded sources in the nearby Taurus star-forming region: TMC-1 (IRAS 04381+2540) and TMC-1A (IRAS 04365+2535). They have the steepest (2–25  $\mu\text{m}$ ) spectral index of the objects in Taurus surveyed in the infra-

<sup>1</sup> Recipient of a NSF CAREER Award.

red by Myers et al. (1987), suggesting that they are two of the youngest and most deeply embedded sources in this region; their luminosities are 0.73 and 2.4  $L_{\odot}$ , respectively. Both objects were originally reported not to have outflows in large-beam, single-dish surveys, but were shown to have high-velocity, compact emission in the interferometer snapshot survey of Terebey, Vogel, & Myers (1989). They are therefore good candidates for having young, compact, unevolved outflows.

To study the energetics of the high-velocity gas in TMC-1 and TMC-1A, and to examine its small-scale structure, we have performed high-resolution imaging of both sources in CO  $J = 1-0$  and  $J = 2-1$ , and in the near-infrared continuum. Below we describe the results and compare our data with predictions from recent outflow models, providing new constraints on the driving mechanism of outflows.

## 2. OBSERVATIONS AND DATA REDUCTION

### 2.1. CO $J = 1-0$ Observations Using the Owens Valley Millimeter Array

Full aperture synthesis maps of TMC-1 and TMC-1A in CO  $J = 1-0$  were made using the Owens Valley Millimeter Array during the period 1988 January–June. The absolute flux scale was established from observations of the planets and results in an estimated uncertainty of 15%. Spectral line data were obtained using a filter bank with 32 channels at 1 MHz ( $2.6 \text{ km s}^{-1}$ ) resolution. After calibration, the data were imaged using the AIPS reduction package. The resolutions (FWHM) of the CO beam made with uniform weighting were  $7.0 \times 6''.8$  at P.A.  $-28^\circ$  for TMC-1A and  $7.3 \times 6''.6$  at P.A.  $8^\circ$  for TMC-1. The rms noise in each channel is  $0.38 \text{ Jy beam}^{-1}$  for TMC-1A and  $0.15 \text{ Jy beam}^{-1}$  for TMC-1.

### 2.2. CO $J = 1-0$ Observations Using the NRAO 12 m Telescope

A single-dish spectrum of the CO  $J = 1-0$  emission from TMC-1A was made in 1991 April using the 12 m telescope of the National Radio Astronomy Observatory<sup>2</sup> at Kitt Peak. The velocity resolution was  $0.127 \text{ km s}^{-1}$  and the beam was  $60''$  at 2.7 millimeters. Monitoring of the pointing and focus showed they were good to 15% and 10%, respectively. The data were corrected for forward scattering and spillover on-line to give spectra of  $T_R^*$ . Observations of the flux calibration source Orion A showed the absolute calibration of  $T_R^*$  was within 10%, and flux repeatability was 5%. Since  $T_R^*$  refers to a source extended relative to the main beam, and the emission from TMC-1A is relatively compact compared with  $60''$  (see § 3), we have further corrected our data to main beam brightness temperature,  $T_{MB}$  by dividing by 0.82 (P. Jewell 1996, private communication).

### 2.3. CO $J = 2-1$ Observations Using the JCMT

The CO  $J = 2-1$  observations of TMC-1 and TMC-1A were carried out at the 15 m James Clerk Maxwell Telescope (JCMT), on Mauna Kea, Hawaii. TMC-1A was observed in 1990 September and TMC-1 in 1991 September. Both sets of observations used the common-user

Schottky receiver and an acousto-optical spectrometer (AOS) with a channel spacing of 250 kHz and a resolution of 330 kHz. The beam width at 230 GHz is about  $21''$ . Typical double-sideband system temperatures were 1000–2000 K. Integration times of around 400 s, including on and off positions, yielded an rms noise (in units of  $T_A^*$ ) of 0.24 K per channel. The pointing was checked using CRL 618 every 1–2 hr, and was found to be good to  $5''$ .

An off position  $10'$  east of the program source was adopted in each case. Since the Taurus cloud is so extended, it is difficult to find a good emission-free region to use as an off position. To maintain reasonable baselines we were restricted to using a position relatively close to each source. There is therefore a serious possibility of emission at the off position. However, since we are interested mainly in the high-velocity emission away from the cloud systemic velocity, we have made no attempt to correct the resulting on-off spectra for emission in the off beam. The maps are fully sampled with a point spacing of  $10''$ . Due to time constraints during the observing, we concentrated on mapping only the main, extended outflow lobe in each source (i.e., the blue lobe in TMC-1A and the red lobe in TMC-1). We also obtained spectra at offsets of  $30''$  from the central source in the direction of the opposite lobe, but no high-velocity emission was found in either case.

The data reduction and image processing were carried out using SPECX and AIPS. In order to compare the single-dish data directly with the interferometer maps, we have converted the JCMT spectra from units of  $T_A^*$  to  $\text{Jy beam}^{-1}$ . A linear baseline has been removed from all the spectra, which have then been corrected for forward scattering and spillover by dividing by  $\eta_{\text{fss}} = 0.8$  to give  $T_R^*$ , and multiplied by  $19 \text{ Jy beam}^{-1} \text{ K}^{-1}$ . The rms noise per channel is therefore  $5.7 \text{ Jy beam}^{-1}$ .

### 2.4. Near-Infrared Imaging at the Hale 5 m Telescope

Near-infrared  $H$ - and  $K$ -band images of TMC-1 and TMC-1A were obtained in 1988 December using the PFIRCAM infrared camera mounted at the prime focus of the Hale 5 m telescope on Mount Palomar. The camera used a  $128 \times 128$  HgCdTe detector array bonded to a Reticon readout and operating between 1 and  $2.5 \mu\text{m}$  with  $0''.765$  pixels. The spatial resolution of the observations, determined by the seeing, was about  $1''.5$ . The data were taken alternating between the source and four different sky positions. The images were bias-subtracted, and then flat-fielded with a median sky frame, using special IDL software developed for PFIRCAM. The total on-source integration times of the final images were 880 s at  $K$  and 240 s at  $H$  for TMC-1, and 1000 s at  $K$  and 1280 s at  $H$  for TMC-1A. The images have also been smoothed to approximately  $2''.5$  resolution. Photometric standards were selected from the CIT system (Elias et al. 1982).

The data were not obtained under photometric conditions. However, the quality is sufficient to study source structure. Careful monitoring of the sky background showed good stability for both TMC-1 and TMC-1A at both  $H$  and  $K$ . A comparison with published fluxes shows agreement within 0.4 magnitudes. Near-infrared images that have been published previously for TMC-1 and TMC-1A (Kenyon et al. 1993b; Tamura et al. 1991) are less sensitive and have lower spatial resolution. The images presented here reveal the underlying structure of the extended nebulosity.

<sup>2</sup> The National Radio Astronomy Observatory is a facility of the National Science Foundation operated under cooperative agreement by Associated Universities, Inc.

## 3. RESULTS

## 3.1. Molecular Line Emission

## 3.1.1. Morphology

In Figures 1 and 2 we compare Owens Valley CO(1–0) channel data with the JCMT CO(2–1) data, which have been averaged over 8 channels to give the same spectral resolution as the interferometer images. The LSR velocity is marked at the top right of each panel in  $\text{km s}^{-1}$ . The position of the millimeter continuum source from Terebey, Chandler, & André (1993) is marked by an asterisk in each image, and the scale is the same in each data set. Both TMC-1 and TMC-1A show distinct red- and blueshifted lobes oriented north-south. Features larger than  $20''$  visible in the single-dish data are resolved out by the interferometer. A comparison with the NRAO 12 m spectrum of TMC-1A shows that the interferometer has resolved out over 50% of the total flux density in the line wings of that source and more than 90% of the flux close to the systemic velocity. Nevertheless, the correspondence between the locations of the small-scale structure in both the JCMT and Owens Valley data sets, in the different transitions of CO, is extremely good. The systemic LSR velocity measured by Terebey et al. (1989) is  $5.5 \text{ km s}^{-1}$  for TMC-1 and  $6.4 \text{ km s}^{-1}$  for TMC-1A.

At high resolution in the interferometer data, the TMC-1A outflow (Fig. 2a) shows the blue lobe at 4–7 km

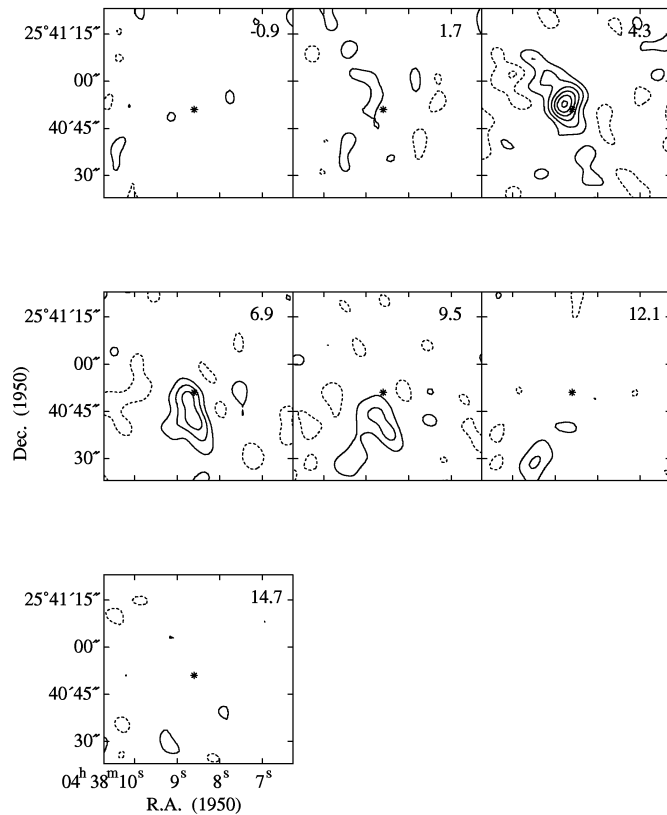


FIG. 1a

$\text{s}^{-1}$  away from the systemic velocity to have a conical structure, with its apex located at the position of the millimeter continuum source. A similar, less extended structure is also seen in the redshifted channel. The red lobe of TMC-1 (Fig. 1a) is also roughly conical, with the highest velocity emission at the largest distance from the source. This is more clearly demonstrated in the CO(2–1) JCMT data (Fig. 1b), where the peak in the emission shifts about  $20''$  south moving from  $V_{\text{LSR}} = 6.8 \text{ km s}^{-1}$  to  $V_{\text{LSR}} = 19.7 \text{ km s}^{-1}$ . This is also seen, to a slightly lesser degree, in the blue lobe of TMC-1A traced by CO(2–1) (Fig. 2b).

The integrated red and blue CO(1–0) emission (Fig. 3) demonstrates the conical structure of the outflow lobes, extending to within 1000 AU of the continuum source. In Figure 4 we directly compare these interferometer results (*gray scale*) with the integrated JCMT CO(2–1) emission (*contours*). All the features in the high-resolution data have corresponding emission in the CO(2–1) maps. The orientation of both outflows is similar, with position angles for the outflow axis of  $0^\circ$  for TMC-1 and  $-10^\circ$  for TMC-1A. Because of their larger spatial coverage and higher spectral resolution, we use the CO(2–1) data to analyze the dynamics of the outflow.

## 3.1.2. Optical Depth and Excitation Temperature of the CO

For TMC-1A we have combined information from the single-dish CO  $J = 1-0$  spectrum, the Owens Valley

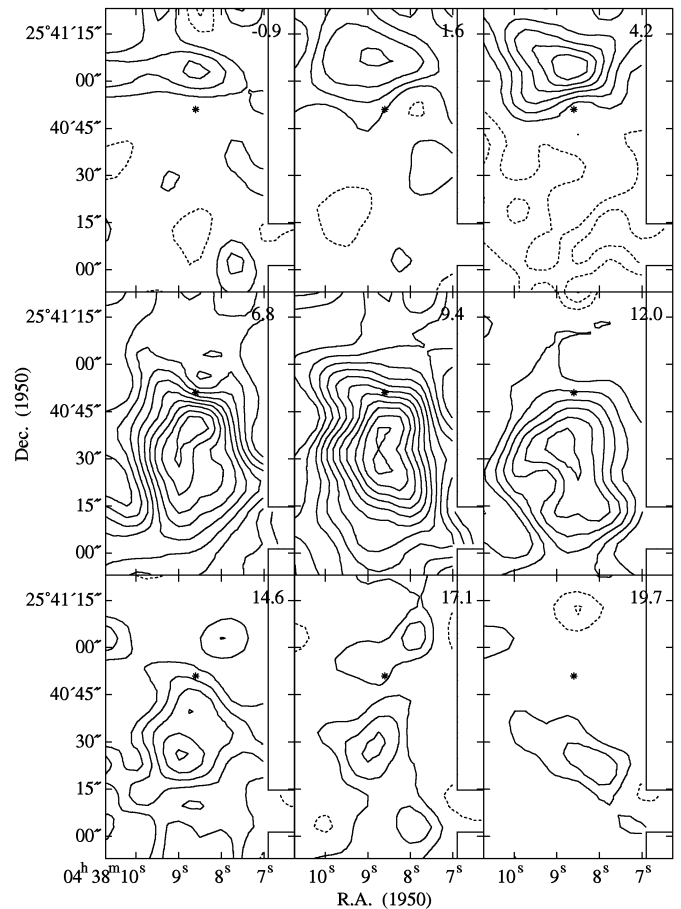


FIG. 1b

FIG. 1.—Channel maps of the CO emission from TMC-1. (a) CO(1–0) imaged with the Owens Valley Millimeter Array. The LSR velocity is given at the top right hand corner of each panel, in  $\text{km s}^{-1}$ . Contours are spaced at  $2\sigma$  intervals of  $0.3 \text{ Jy beam}^{-1}$ , starting at  $0.3 \text{ Jy beam}^{-1}$ . The asterisk denotes the continuum position given in Terebey et al. (1993). (b) CO(2–1) emission obtained with the JCMT plotted to the same scale as the interferometer data, in the same velocity intervals. Contours are spaced at  $2\sigma$  intervals of  $4 \text{ Jy beam}^{-1}$ , from a base level of  $4 \text{ Jy beam}^{-1}$ .

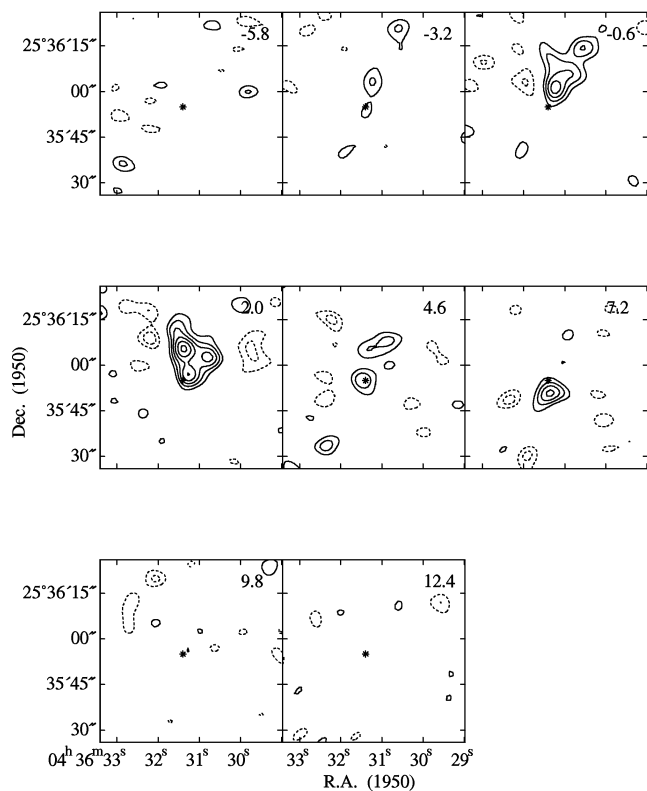


FIG. 2a

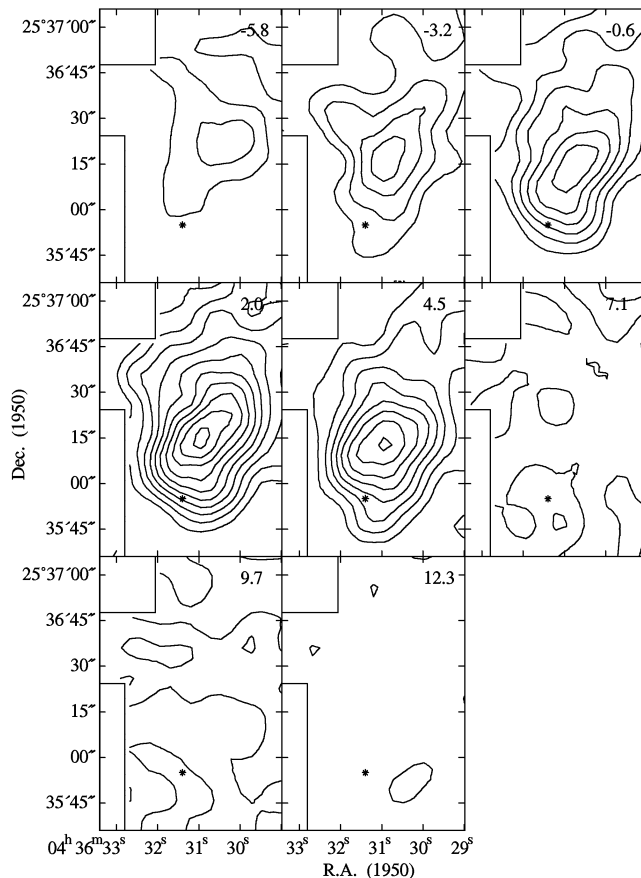


FIG. 2b

FIG. 2.—Same as Fig. 1, for TMC-1A. (a) CO(1-0) imaged with the Owens Valley Millimeter Array. Contours are spaced at  $1 \sigma$  intervals of  $0.4 \text{ Jy beam}^{-1}$ , starting at the  $2 \sigma$  level of  $0.8 \text{ Jy beam}^{-1}$ . The asterisk is the position of the continuum source from Terebey et al. (1993). (b) CO(2-1) emission from the JCMT. Contours are spaced at  $3 \sigma$  intervals of  $6 \text{ Jy beam}^{-1}$ , starting at  $6 \text{ Jy beam}^{-1}$ .

images, and the  $J = 2-1$  data to derive constraints on the optical depth and the excitation temperature of the CO emission in the outflow wings. First, consider the two single-dish data sets. The CO(1-0) spectrum obtained using

the NRAO 12 m has been smoothed and resampled to have the same spectral resolution as the  $J = 2-1$  JCMT data, while the 2-1 data has been smoothed spatially to match the 12 m beam. The resulting spectra are displayed in

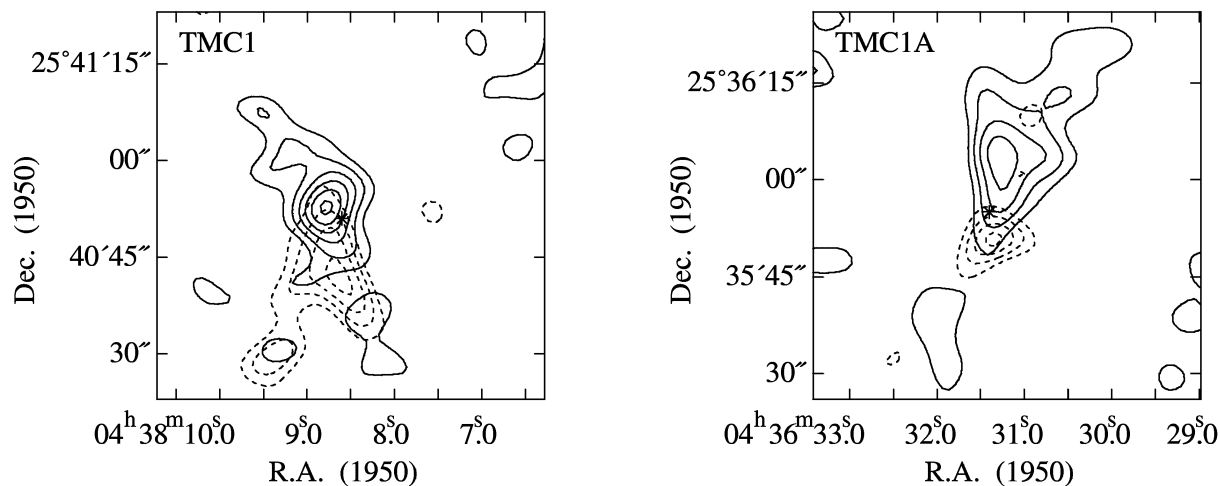


FIG. 3.—Interferometer maps of the integrated red- and blueshifted CO(1-0) emission from TMC-1 (left) and TMC-1A (right), demonstrating the conical structure of the outflow lobes. The blueshifted gas is denoted by the solid contours, and the redshifted gas is plotted as dashed contours. For TMC-1, the blueshifted emission is the  $4.3 \text{ km s}^{-1}$  ( $V_{\text{LSR}}$ ) channel, with contours spaced at  $0.3 \text{ Jy beam}^{-1}$ . The redshifted emission is an average of the three channels at 6.9, 9.5, and  $12.1 \text{ km s}^{-1}$ , with contours  $1.5 \sigma$  intervals of  $0.13 \text{ Jy beam}^{-1}$ , starting at the  $3 \sigma$  level of  $0.26 \text{ Jy beam}^{-1}$ . For TMC-1A, the blueshifted emission is an average of the three channels at  $-3.2$ ,  $-0.6$  and  $2.0 \text{ km s}^{-1}$  ( $V_{\text{LSR}}$ ), with contours spaced at  $0.4 \text{ Jy beam}^{-1}$ , starting at  $0.4 \text{ Jy beam}^{-1}$ , and the redshifted emission is the  $7.2 \text{ km s}^{-1}$  with contours as in Fig. 2.

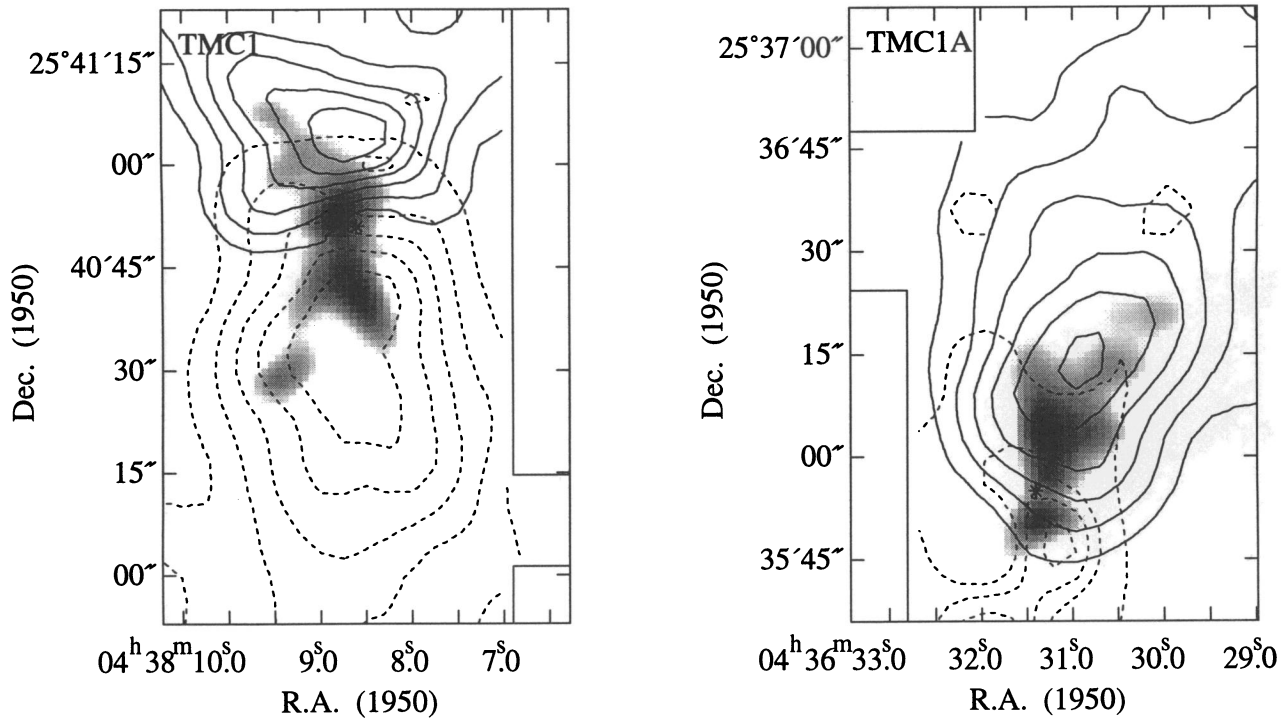


FIG. 4.—Integrated blue- and redshifted CO(2–1) emission, overlaid on a gray-scale image of the high-velocity gas imaged by the interferometer in CO(1–0). The velocity intervals for the integration are the same as in Fig. 3. Contour levels for the TMC-1 blue lobe are the same as in Fig. 1; contour levels for the red lobe are at  $5\sigma$  intervals of  $6 \text{ Jy beam}^{-1}$ . For TMC-1A the blue contours are at intervals of  $8 \text{ Jy beam}^{-1}$ , and the red contours are at 30, 37, 40, and  $43 \text{ Jy beam}^{-1}$ .

Figure 5, with a dotted line denoting the (2–1)/(1–0) line ratio ( $T_{21}/T_{10}$ ) in the region where the signal-to-noise ratio was greater than unity in both transitions. In the line wings  $T_{21}/T_{10}$  has a mean value of 2.3, or equivalently, a flux density ratio  $S_{21}/S_{10}$  of 9.3. This can be translated into a lower limit to the excitation temperature in the high-velocity gas by assuming LTE and optically thin emission. Figure 6 shows the predicted value of  $S_{21}/S_{10}$  as a function of  $T_{\text{ex}}$  for various optical depths in the  $J = 1-0$  line,  $\tau_{10}$ , assuming LTE (note that  $\tau_{21} > \tau_{10}$  as long as  $T_{\text{ex}} > 5.5 \text{ K}$ ). In the optically thin limit the minimum excitation temperature that can be responsible for the observed flux density ratio, denoted by the dotted line, is 20 K. This temperature is somewhat higher than the  $\sim 10 \text{ K}$  observed for the bulk of the Taurus molecular cloud (Murphy & Myers 1985).

Further constraints on the excitation conditions on the scales imaged by the interferometer can be obtained by comparing the flux density in the Owens Valley CO(1–0) maps with the CO(2–1) data. For TMC-1A, the average ratio  $S_{21}/S_{10}$  in the line wings integrated over the area of emission in the Owens Valley maps is approximately 6 (solid circle, Fig. 6). Since the interferometer flux density is a lower limit, this line ratio is an upper limit to the true line ratio on small scales. The difference between the line ratios derived from the large-scale, single-dish data and those obtained from the interferometer measurements reflects the different gas components sampled by the various instruments. It demonstrates that the more extended emission to which the interferometer is not sensitive, but which is detected by the NRAO 12 m and the JCMT, either has a higher excitation temperature or is more optically thin than the compact structures. Since there is no reason to believe that the gas observed by the Owens Valley array is cooler

than the material on larger scales, we assume that the result  $T_{\text{ex}} \gtrsim 20 \text{ K}$  derived above from the large-scale emission can be applied to the more compact structures. An examination of Figure 6 then shows that the emission in both the 1–0 and 2–1 transitions must be optically thick in TMC-1A. For TMC-1 the ratio  $S_{21}/S_{10} \sim 10$ , so either  $T_{\text{ex}} > 23 \text{ K}$ , or the interferometer has resolved out too much emission for a reasonable comparison between the two lines to be made. The latter is most likely to be the case.

The peak brightness temperature of the line wings in our data set is 6 K and lies in the Owens Valley CO(1–0) map of TMC-1A at  $V_{\text{LSR}} = 2.0 \text{ km s}^{-1}$ . Since the excitation temperature is probably greater than 20 K and the emission is optically thick, the observed brightness temperature implies that the emission in the outflow is clumpy even with respect to the interferometer beam.

### 3.1.3. Outflow Properties

In LTE the total mass  $M$  of molecular material is obtained from the CO(2–1) emission using the relation

$$M = 2.9 \times 10^{-8} (T_{\text{ex}} + 0.9) e^{16.6/T_{\text{ex}}} \times \frac{\tau_{21}}{(1 - e^{-\tau_{21}})} \left( \frac{D}{140 \text{ pc}} \right)^2 \int S dV M_{\odot}. \quad (1)$$

Equation (1) assumes a mean molecular weight for the molecular gas of 1.36, and a CO abundance relative to  $\text{H}_2$  of  $10^{-4}$ .  $D$  is the distance to the source, and the integrated CO(2–1) flux is in units of  $\text{Jy km s}^{-1}$ . In calculating the mass of molecular material we have assumed  $T_{\text{ex}} = 20 \text{ K}$  and  $\tau_{21} \ll 1$ . These values for the mass should therefore be regarded as lower limits since it is likely that  $T_{\text{ex}} > 20 \text{ K}$  and that the  $J = 2-1$  emission is optically thick.

The detailed modeling reported by Cabrit & Bertout

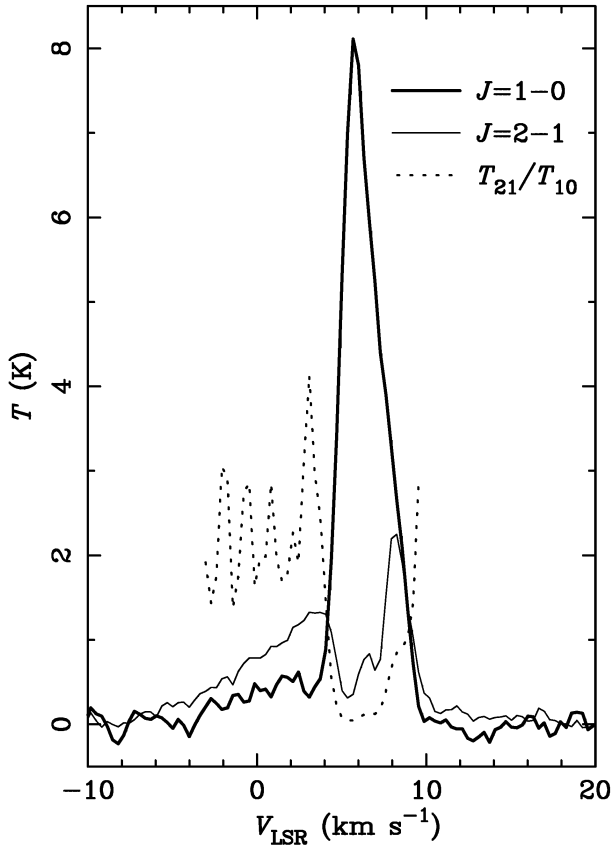


FIG. 5.—Spectra of TMC-1A in CO  $J=1-0$  (thick line) and  $J=2-1$  (thin line). The  $1-0$  line is the spectrum obtained from the NRAO 12 m, and the  $2-1$  is data obtained using the JCMT smoothed to the same spatial resolution. The dotted line is the ratio of  $2-1/1-0$  for those channels where the signal-to-noise ratio in both transitions was greater than unity.

(1990) suggests that the best estimates for the properties of an outflow are obtained by (1) calculating the mass correcting for the line opacity, and (2) assuming that all the material is moving at  $V_{\max}$ , the maximum projected radial velocity observed, rather than the intensity-weighted velocity,  $\langle V \rangle$ . Since we do not know the opacity of the  $J=2-1$  emission, we have not applied any opacity correction. In Table 1 we list the dynamical timescale  $t_{\text{dyn}}$ , the momentum  $P$ , momentum flux  $F$ , energy  $E$ , mechanical luminosity  $L$ , and mass-loss rate  $\dot{M}_{\text{outflow}}$  using  $V_{\max}$ . Detectable emission in the “red lobe” of TMC-1 lies between 7.9 and 20.9 km

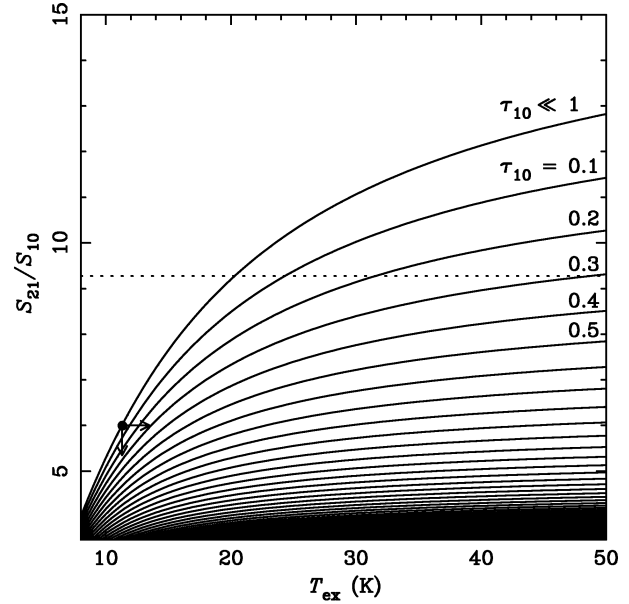


FIG. 6.—Plot of the flux density ratio in the  $J=2-1$  and  $1-0$  transitions of CO,  $S_{21}/S_{10}$ , as a function of excitation temperature in LTE for various values of the  $J=1-0$  optical depth. No solutions are possible for the line ratio in the region above the optically thin limit. The dotted line shows the line ratio measured from the NRAO 12 m/JCMT data for TMC-1A, and the solid circle is the value obtained on much smaller scales from the JCMT and the Owens Valley interferometer measurements.

$s^{-1}$  and in the “blue lobe” between  $-3.7$  and  $3.4$  km  $s^{-1}$ . For TMC-1A the red lobe is from  $7.9$  to  $18.3$  km  $s^{-1}$  and the blue lobe from  $-7.2$  to  $3.1$  km  $s^{-1}$ . The extent  $R$  of the outflows listed in Table 1 may be larger than the area we have mapped. Many of the quantities derived are therefore limits, although emission is clearly falling off at the edge of our maps. The outflows cannot extend more than  $2R$  because high-velocity gas was not detected in the lower resolution survey of Heyer et al. (1987).

Cabrit & Bertout (1990) also calculate the error introduced by calculating outflow parameters, while not correcting for the opacity of the CO line or inclination angle. In Table 2 we show the average error for an intermediate viewing angle,  $i \sim 30^\circ-60^\circ$ . Applying these corrections to our data, the outflow momentum fluxes for TMC-1 and TMC-1A are in excellent agreement with those predicted by the correlation between bolometric luminosity and outflow momentum flux and mechanical luminosity found by

TABLE 1  
OUTFLOW PROPERTIES DERIVED FROM CO(2-1) DATA

PARAMETER	TMC-1		TMC-1A	
	Red Lobe	Blue Lobe	Red Lobe	Blue Lobe
$M (M_\odot)$ .....	$1.2 \times 10^{-3}$	$2.5 \times 10^{-4}$	$9.0 \times 10^{-4}$	$1.5 \times 10^{-3}$
$V_{\max} (\text{km s}^{-1})^a$ .....	15.4	9.2	11.9	13.6
$\langle V \rangle (\text{km s}^{-1})^a$ .....	5.9	4.1	3.1	6.7
$R(\text{m})$ .....	$1.3 \times 10^{15}$	$6.3 \times 10^{14}$	$3.2 \times 10^{14}$	$1.6 \times 10^{15}$
$t_{\text{dyn}} = R/V_{\max} (\text{yr})$ .....	2600	2200	840	3700
$P = MV_{\max} (M_\odot \text{ km s}^{-1})$ .....	$1.8 \times 10^{-2}$	$2.3 \times 10^{-3}$	$1.1 \times 10^{-2}$	$2.0 \times 10^{-2}$
$F = MV_{\max}^2/R (M_\odot \text{ km s}^{-1} \text{ yr}^{-1})$ .....	$7.1 \times 10^{-6}$	$1.0 \times 10^{-6}$	$1.3 \times 10^{-5}$	$5.5 \times 10^{-6}$
$E = MV_{\max}^3/2 (\text{J})$ .....	$2.8 \times 10^{35}$	$2.1 \times 10^{34}$	$1.3 \times 10^{35}$	$2.8 \times 10^{35}$
$L = MV_{\max}^3/2R (L_\odot)$ .....	$8.8 \times 10^{-3}$	$7.8 \times 10^{-4}$	$1.2 \times 10^{-2}$	$6.1 \times 10^{-3}$
$\dot{M}_{\text{outflow}} = MV_{\max}^2/R (M_\odot \text{ yr}^{-1})$ .....		$6 \times 10^{-7}$		$1.5 \times 10^{-6}$

<sup>a</sup> Assumes systemic velocity of 5.5 and 6.4 km  $s^{-1}$  for TMC-1 and TMC-1A, respectively.

TABLE 2  
 OUTFLOW PROPERTIES CORRECTED FOR ERRORS INTRODUCED DUE TO THE LACK OF AN  
 OPACITY CORRECTION<sup>a</sup>

QUANTITY $X$	LOG ( $X_{obs}/X_{cor}$ )	$X_{obs}$		$X_{cor}$	
		TMC-1	TMC-1A	TMC-1	TMC-1A
$M (M_{\odot})$ .....	-0.80	$1.5 \times 10^{-3}$	$2.4 \times 10^{-3}$	$9.5 \times 10^{-3}$	$1.5 \times 10^{-2}$
$P (M_{\odot} \text{ km s}^{-1})$ .....	-0.55	$2.0 \times 10^{-2}$	$3.1 \times 10^{-2}$	$7.1 \times 10^{-2}$	$1.1 \times 10^{-1}$
$F (M_{\odot} \text{ km s}^{-1} \text{ yr}^{-1})$ .....	-0.55	$8.1 \times 10^{-6}$	$1.8 \times 10^{-5}$	$2.9 \times 10^{-5}$	$6.4 \times 10^{-5}$
$E (J)$ .....	-0.35	$3.0 \times 10^{35}$	$4.1 \times 10^{35}$	$6.7 \times 10^{35}$	$9.2 \times 10^{35}$
$L (L_{\odot})$ .....	-0.60	0.010	0.018	0.038	0.072

<sup>a</sup> Based on the models of Cabrit & Bertout 1990.

Cabrit & Bertout (1992). The uncorrected mass-loss rates listed in Table 1 are  $\sim 0.1 \dot{M}_{infall}$  derived from the near-infrared colors of TMC-1 and TMC-1A by Kenyon et al. (1993b).

3.2. Near-Infrared Imaging

The results of imaging TMC-1 and TMC-1A at  $H$  and  $K$  are displayed as contours in Figure 7, overlaid on gray

scales of the integrated CO(1-0) emission in Figure 3. The structures we see in our  $K$  images are in good agreement with the lower sensitivity data presented by Kenyon et al. (1993b), but we have clearly detected more of the low-level, extended nebulosity. There is an unresolved component of the near-infrared emission which we have aligned with the position of the millimeter continuum source at the geometrical center of the outflow since we do not have good

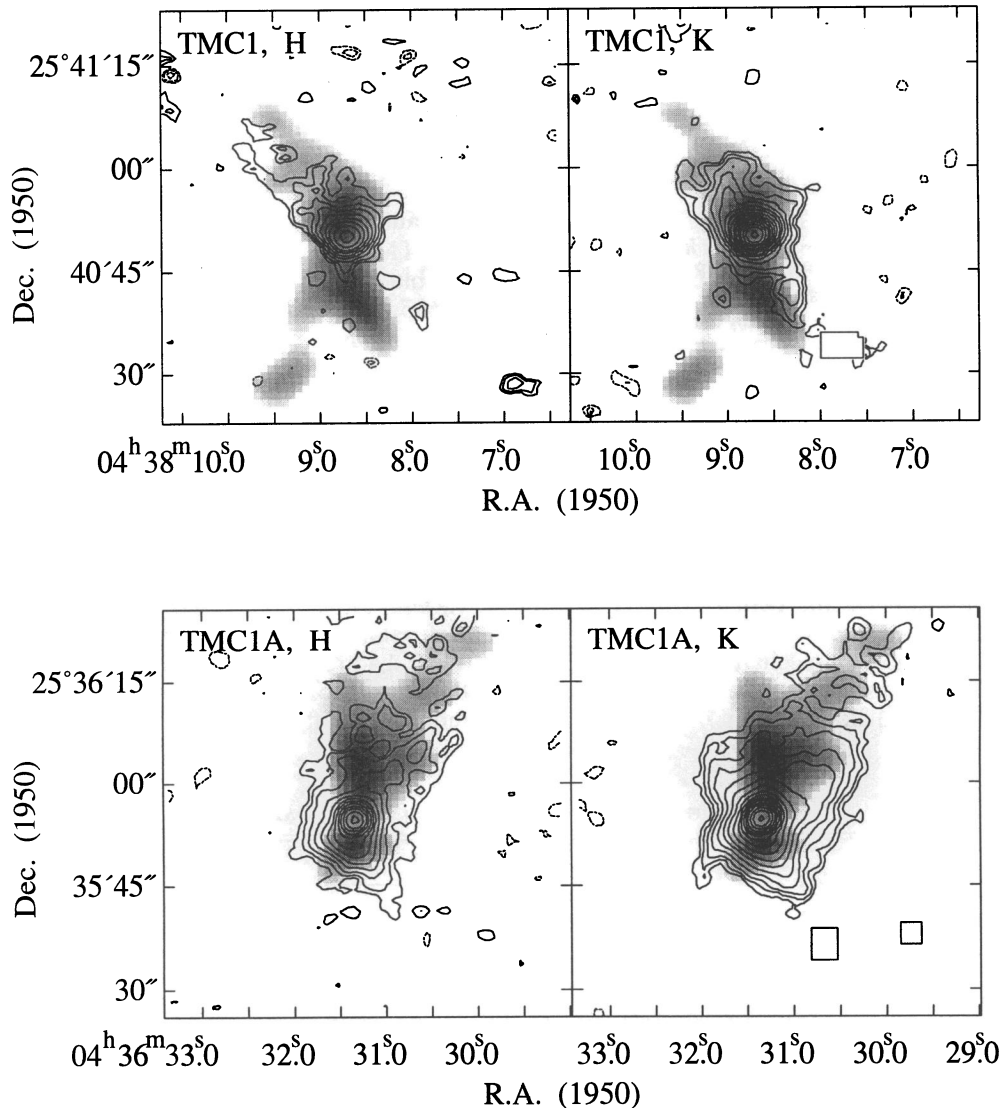


FIG. 7.—Contour plots of the near-infrared emission from TMC-1 (top) and TMC-1A (bottom) overlaid on gray-scale images of the integrated high-velocity CO emission shown in Fig. 3. On the left for each source is the  $H$  ( $1.6 \mu\text{m}$ ) continuum, and on the right is the  $K$  ( $2.2 \mu\text{m}$ ) continuum. The flux densities have been normalized to the photometry measured by Kenyon et al. (1993b), and contour levels are logarithmic at intervals of  $\pm 1.5^n \times 2.7 \mu\text{Jy arcsec}^{-2}$  (TMC-1,  $H$  band),  $3.1 \mu\text{Jy arcsec}^{-2}$  (TMC-1,  $K$  band),  $4.1 \mu\text{Jy arcsec}^{-2}$  (TMC-1A,  $H$  band), and  $8.4 \mu\text{Jy arcsec}^{-2}$  (TMC-1A,  $K$  band), where  $n = 0, 1, 2, 3, \dots$

absolute positions for the infrared measurements. The extended emission can be divided into two components. Close to the star it is roughly symmetric, while at larger distances it has more of the appearance of a unipolar reflection nebula. The most striking result demonstrated by Figure 7 is how well this extended emission corresponds to the blueshifted outflow emission for both sources.

The structure of the near-infrared emission is in excellent agreement with Monte Carlo simulations of scattered light from embedded stars (Whitney & Hartmann 1993; Kenyon et al. 1993b). Furthermore, our images clearly demonstrate the need for a hole or cavity to explain the extent and shape of the emission in the context of their model. We have used the photometry measured by Kenyon et al. to calibrate our images and convert them to  $F_\nu$  and find that the extended nebulosity in both sources has an intensity ratio  $r = I_K/I_H \lesssim 2$ , corresponding to a blackbody temperature  $T \gtrsim 1500$  K. Since these are low-luminosity objects the high color temperatures located at 3000–4000 AU from the central star cannot represent the physical temperature of dust at such large distances; the extended emission is most likely to be reflection nebulosity (Heyer et al. 1990; Tamura et al. 1991; Kenyon et al. 1993b).

In TMC-1A there is also emission at  $K$  along the north-western edge of its nebula without corresponding features at  $H$ , giving  $r \sim 12$ , and resulting in a lower color temperature of  $\sim 700$  K at that location. Variations in the color temperature across near-infrared nebulae could be caused by two effects. First, clumpiness in the foreground extinction will have a correspondingly higher effect at  $H$  band than at  $K$ : the extinction law of Rieke & Lebofsky (1985) suggests that a  $K$ -band extinction  $A_K \sim 3.2$  is needed to make an intrinsic intensity ratio of 2 appear as high as 12. Alternatively the variation in color temperature may be caused by variations in the emission mechanism across the nebula. Low values of  $r$  (and correspondingly high  $T$ ) may be located in regions where the emission is predominantly reflection nebulosity, while higher intensity ratios may indicate regions of shock-heated gas, with  $H_2$  emission contributing to the  $K$ -band flux density. Such shocks could occur where a jet or wind driving the outflow interacts with the ambient cloud. Whatever their cause, the red knots located to the west and northwest of the star in TMC-1A may account for the apparent increase in the  $H-K$  and  $J-K$  colors with increasing aperture size reported by Kenyon et al. (1993b) for this source.

It is interesting to note that where near-infrared emission is detected toward the red outflow lobe of both objects, the color of the nebulosity is similar to that in the blue. This indicates that the lack of extended emission toward the red lobe is not due to an increase in the large-scale extinction, but must be caused either by a lack of material in the south to scatter radiation, or by the effect of forward scattering of the dust grains. The former may play an important role in TMC-1A, where we see little molecular line emission to the south. For TMC-1, however, there is clearly extended molecular gas, suggesting that forward scattering is the dominant process causing the asymmetry of the red and blue lobes in the reflection nebula.

### 3.3. Outflow Geometry and Orientation

The semi-opening angle of the outflow,  $\theta_{\max}$ , can potentially provide important constraints on outflow models. For TMC-1 and TMC-1A the well-delineated conical structure

permits precise measurement of  $\theta_{\text{proj}}$ , the projected semi-opening angle. We find  $\theta_{\text{proj}} = 20^\circ \pm 2^\circ$  for the red lobe in TMC-1, and  $\theta_{\text{proj}} = 22^\circ \pm 2^\circ$  for the blue lobe of TMC-1A. If the wind cone is azimuthally symmetric, then it is straightforward to show that

$$\tan(\theta_{\max}) = \tan(\theta_{\text{proj}}) \sin i, \quad (2)$$

where  $i$  is the inclination of the axis of symmetry to the line of sight. Values of  $\theta_{\max}$  derived from equation (2) are plotted for  $\theta_{\text{proj}} = 20^\circ$  (labeled TMC-1) and  $\theta_{\text{proj}} = 22^\circ$  (labeled TMC-1A) in Figure 8. We plot  $\theta_{\max}$  as a function of  $1 - \cos i$ , since the probability of finding a source with inclination  $i$  is proportional to  $\sin i$  and the probability distribution function is therefore proportional to  $1 - \cos i$ . For this choice of independent variable, equal intervals along the horizontal axis will have the same probability. Random orientations should therefore result in equal numbers of outflows below and above  $60^\circ$  inclination. Figure 8 demonstrates that the wind opening angle is always smaller than or equal to the projected opening angle, although the difference is primarily important for small inclinations.

The wind opening angle may therefore be computed once the inclination is known. Outflow inclinations have, however, been difficult to measure securely. Outflows that are highly inclined ( $i \geq 75^\circ$ ) and lie nearly in the plane of the sky are readily identified by their characteristic pattern of overlapping red and blue shifted gas (case 3 in Fig. 8), as discussed by Cabrit & Bertout (1986). Less inclined outflows present greater ambiguity, which partly explains why few reliable inclinations exist in the literature.

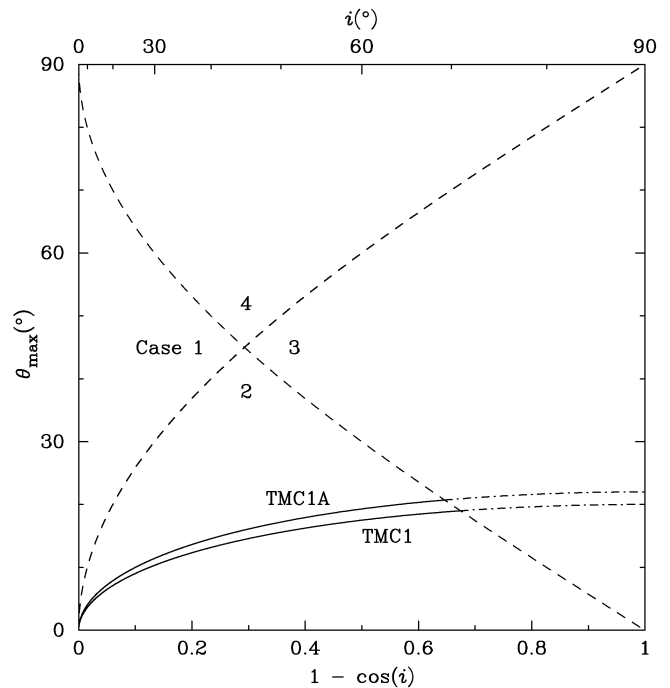


FIG. 8.—Plot of the probability of different outflow geometries occurring for different combinations of inclination angle,  $i$ , and semi-opening angle,  $\theta_{\max}$ . The geometries for cases 1, 2, 3, and 4 are defined by Cabrit & Bertout (1986) and are described in the text. The probability of observing a particular inclination for randomly oriented outflows is proportional to  $1 - \cos i$ . The two lines marked TMC-1 and TMC-1A show the solution of equation (2) for  $\theta_{\text{proj}} = 20^\circ$  (TMC-1) and  $\theta_{\text{proj}} = 22^\circ$  (TMC-1A).



### 3.3.1. Comparison with CO Spectral Line Outflow Models

One method of assessing inclination and opening angles of outflows compares molecular spectral line data to theoretical models. Cabrit & Bertout (1986, 1990) present models of the CO spectral line emission predicted from conical outflows. Figure 8 shows the regimes which correspond to the four different cases defined by Cabrit & Bertout. Case 3 outflows lie in the plane of the sky, while case 2 outflows have distinct redshifted and blueshifted lobes, well-separated spatially. Case 1 outflows are observed almost pole-on, and the redshifted and blueshifted lobes overlap. Case 4 outflows, which have very large opening angles, are rarely, if ever, observed. Cabrit & Bertout (1986) calculate the probability of observing an outflow with a given  $\theta_{\max}$ , and show that for  $\theta_{\max} \lesssim 20^\circ$  (as is observed for TMC-1 and TMC-1A) the highest probability is found for case 2. This is also demonstrated in Figure 8 by the possible solutions for those flows in the case 2 region of the plot compared with cases 1 and 3.

It is therefore most probable that TMC-1 and TMC-1A have case 2 outflows, and to test this possibility further we compare CO position-velocity (P-V) diagrams obtained along the outflow axis with the theoretical diagrams calculated by Cabrit & Bertout (1986, 1990). Figure 9 shows the P-V diagrams obtained from our 8 channel averaged JCMT data, together with full resolution CO(2-1) spectra averaged over the mapped area to demonstrate the shape of the line wings. Close to the systemic velocity (marked by the *solid vertical line*) in both sources a combination of self-

absorption by cool foreground material and emission in our off positions serve to produce an artificial valley of low flux density.

Both our P-V diagrams and the integrated line profile correspond most closely to the case 2 models for an accelerated flow (Cabrit & Bertout 1986). Case 2 is defined by the geometrical constraints  $i > \theta_{\max}$ , which gives spatially separated red and blue outflow lobes, and  $i \leq \pi/2 - \theta_{\max}$ , which constrains the flow to lie completely out of the plane of the sky. The source inclinations and opening angles that satisfy both equation (2) and case 2 appear as solid lines in Figure 8. The CO P-V diagrams allow us to exclude inclinations higher than  $70^\circ$  and  $68^\circ$  for TMC-1 and TMC-1A, respectively.

Cabrit & Bertout (1986, 1990) also compute maps of the integrated CO emission. We have not used these images to constrain further the inclination of TMC-1 and TMC-1A since we suspect that the computed spatial distributions may be sensitive to the outer cutoff radius assumed for the outflow cone. For example, an intrinsically short outflow length could be mistaken for a low inclination angle.

### 3.3.2. Comparison with Near-Infrared Scattering Outflow Models

Models of scattered near-infrared emission around protostars have successfully reproduced the observed conical structures (Whitney & Hartmann 1993). The models are sensitive to inclination and may therefore be employed to constrain further the inclination. Whitney & Hartmann present model images that explore the effects of wind,

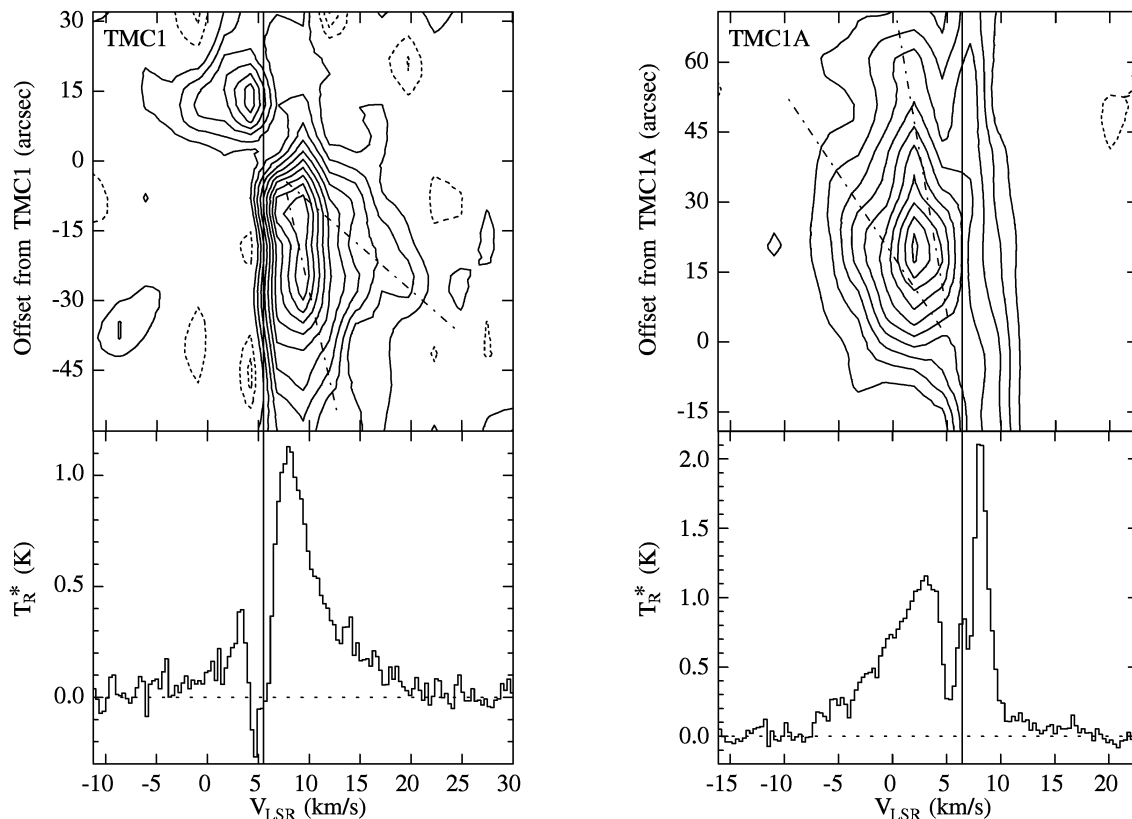


FIG. 9.—Position-velocity diagrams from the 8 channel averaged JCMT CO(2-1) data obtained along the outflow axis for each source. Contours are equally spaced at  $4 \text{ Jy beam}^{-1}$  for TMC-1, and  $6 \text{ Jy beam}^{-1}$  for TMC-1A. The dot-dashed lines in each diagram denote features which correspond to the front and back side of each lobe. Spectra averaged over the whole mapped field with the full spectral resolution of the JCMT data are presented at the bottom of each plot, with solid vertical lines showing the systemic LSR velocity of the cloud in each case.

envelope, and disk geometry on the structure of the near-infrared emission. There are three broad categories: low inclination objects dominated by a central point source similar to case 1, moderate inclination sources displaying unipolar infrared reflection nebulae, and high inclination objects with bipolar infrared reflection nebulae similar to case 3. The near-infrared data for TMC-1 and TMC-1A correspond most closely to their models 5–10 at  $\sim 70^\circ$  inclination. In general, the model images demonstrate very strong asymmetry at moderate inclinations. For  $i < 65^\circ$  they find only the near-side (blue) lobe is visible. Our near-infrared data imply a slightly higher inclination because although the blueshifted lobe is brightest, emission from both lobes is clearly present.

The near-infrared models, combined with the previous constraints, suggest TMC-1 and TMC-1A have inclinations between  $65^\circ$  and  $70^\circ$ . However, the near-infrared constraints are sensitive to the assumed density distribution of the circumstellar material, and the models rely upon high opacity in the envelope to attenuate emission from the far-side (red) lobe. The observed structure of the nebula and the infrared colors of the star could probably also be reproduced at other inclinations (1) by lowering the envelope opacity while increasing the extinction to the central star with a thick disk, or (2) by assuming nonzero opacity within the stellar wind cavity. We therefore adopt  $i > 40^\circ$  as a conservative lower limit to our source inclinations. We conclude that the inclination of TMC-1 is in the range of  $40^\circ$ – $70^\circ$ , which implies a semi-opening angle of  $13^\circ$ – $19^\circ$ . Similarly, the inclination of TMC-1A is  $40^\circ$ – $68^\circ$ , implying a semi-opening angle of  $15^\circ$ – $21^\circ$ . The high ends of the limits are preferred by the models and also by the statistical likelihood of a given inclination.

Several previous estimates of the inclinations of TMC-1 and TMC-1A also exist. The spectral energy distribution analysis carried out by Kenyon, Calvet, & Hartmann (1993a) suggests inclination angles of  $30^\circ$  and  $60^\circ$  for TMC-1 and TMC-1A, respectively, while Kenyon et al. (1993b) prefer inclination angles of  $60^\circ$ – $90^\circ$  for both objects, based on their scattered light imaging and near-infrared colors. This latter near-infrared study is consistent with our near-infrared discussion above. However, the fact that our deeper near-infrared images do not exhibit strongly bipolar structure, along with the spectral line P-V diagram constraints, allow us to rule out very high inclinations.

### 3.4. *The Outflow Cavity*

Comparison of the data with the models shows several interesting features. First, the near-infrared images show limb-brightening that outlines the conical outflow cavity. Whitney & Hartmann (1993) suggest this effect can be produced by curvature in the cavity walls. Second, there is a notable difference between the theoretical P-V diagrams of Cabrit & Bertout (1986) and our data. Figure 9 shows components associated with the front and back sides of each lobe, indicated by dot-dashed lines. Emission at intermediate velocities is apparently suppressed, resulting in concave rather than convex contours. The modeling of Cabrit & Bertout (1986, 1990) assume the lobes are filled with gas, and so do not show these features. This further supports the suggestion that the lobes are evacuated of molecular material, in agreement with our near-infrared imaging. Third, the projected opening angle seen in the near-infrared images is larger than that found in the CO

maps, particularly for TMC-1A. This is in qualitative agreement with the Whitney & Hartmann models, which show the reflection nebosity to be larger than the (assumed) evacuated outflow cavity. More detailed modeling should be useful to constrain the ratio of the density inside and outside the outflow cavity.

## 4. DISCUSSION

### 4.1. *Conical Structure*

Molecular outflows vary greatly in their structure and physical characteristics, but they exhibit many common properties which theoretical outflow models must try to explain (Lada 1985; Masson & Chernin 1993; Stahler 1993). The conical shape near the central star displayed by TMC-1 and TMC-1A (§ 3.1) is a relatively new feature, in part due to the small numbers of objects which have been imaged in CO by millimeter interferometers and the need to observe the youngest protostars.

Conical outflow structure is observed toward the class 0 source B335 in interferometer images (Chandler & Sargent 1993) and on a larger scale in single-dish maps (Hirano et al. 1988). More recently, Bachiller et al. (1995) discovered the class 0 source L1448-C exhibits a conical outflow cavity. L1448-C also has a molecular jet (Bachiller et al. 1990), which makes its similarity to TMC-1 and TMC-1A all the more interesting. However, TMC-1 and TMC-1A have much weaker outflows, reflecting a factor of 3–4 smaller linear extent and velocity and a factor of 10–20 lower mass than the L1448-C molecular jet source.

The age of TMC-1 and TMC-1A with respect to B335 and L1448-C is uncertain, but is important for comparison with theoretical outflow models. André et al. (1993) argue that class 0 sources such as B335 and L1448-C are younger on average than class I sources. However, TMC-1 and TMC-1A are extreme class I sources, which in this interpretation suggests their ages are not too much older than B335 and L1448-C, and probably no more than  $10^5$  yr.

Other young low-mass sources observed in CO with interferometers include L1681B, which shows a low-velocity jet, and L1262 and TMR-1, which have more complex, less collimated structure (Terebey et al. 1990; Terebey, Vogel, & Myers 1989, 1992). The high collimation of L1681B suggests it is very young, an interpretation consistent with its status as an extreme class I source. However, the properties of L1262 and TMR-1 suggest they are older, as has been argued by Bontemps et al. (1996). Taken together the observations imply that outflow cones are associated with the youngest protostars, and moreover, the limited statistics suggest conical structure is a common feature.

### 4.2. *Evacuated Cavity*

The close correspondence of our near-infrared images with scattered light models that show large extended structures (Whitney & Hartmann 1993) provides the most convincing evidence for evacuated outflow cavities. In a near-infrared survey of the Taurus molecular cloud, Kenyon et al. (1993b) argue that most embedded sources have low-opacity outflow cavities. Comparison of our much deeper near-infrared images for TMC-1 and TMC-1A, which clearly show spatially extended conical structure, with the scattering models of Whitney & Hartmann makes this interpretation compelling (§§ 3.2 and 3.3.2) and further bolsters the contention that most embedded sources have

evacuated outflow cavities. The evidence for evacuated cavities from molecular line data has been more controversial (Stahler 1993). However, in the case of TMC-1 and TMC-1A, the P-V diagrams of the CO(2-1) data are consistent with the interpretation of an evacuated outflow cavity (§ 3.3.1).

The outflow cavity is evacuated in the sense that  $\tau_{\text{IR}} \ll 1$  in the outflow, compared with  $\tau > 1$  in the surrounding ambient gas. This suggests that the cavity is filled with low-density material. Alternatively, since dust provides the opacity, the outflow cavity could be filled by a high-density but dust-free jet/wind. In this case, the near-infrared observations place strong constraints on the possible entrainment of ambient cloud material and appear to rule out classes of models which turbulently mix ambient gas/dust into the outflow cavity, producing a filled rather than evacuated outflow cavity (Cantó & Raga 1991; Stahler 1994).

#### 4.3. Moderate Opening Angles

For TMC-1 and TMC-1A, the deprojected full-opening angles of the outflow cones are in the range  $30^\circ$ – $40^\circ$ . There are also reliable opening angles in the literature for several systems whose high inclinations guarantee small deprojection corrections. The class 0 sources B335 and L1448-C both have  $\sim 45^\circ$  opening angles (Chandler & Sargent 1993; Bachiller et al. 1995). Observations of the prototypical class 0 source VLA 1623, also a molecular jet source, show a narrow  $20^\circ$ – $30^\circ$  outflow opening angle (André et al. 1990). For sources showing conical structure, which permits precise measurement of the opening angle, the data suggest typical values of  $30^\circ$ – $45^\circ$  for the outflow opening angle. These values are significantly larger than the predictions of jet-driven outflow models (Masson & Chernin 1993).

#### 4.4. CO Line Profile

The analyses of both Masson & Chernin (1992) and Stahler (1994) use the observed form of mass as a function of velocity  $dM/dV \propto V^\gamma$ , where  $\gamma \sim -1.8$ , to constrain the

swept-up outflow model and the jet entrainment model. Indeed, the fact that the power-law index  $\gamma$  is similar in the sources measured so far, L1551-IRS 5, NGC 2071, HH 46-47 and VLA 1623, has been used as an argument that the same acceleration mechanism is at work in those objects. Extending this analysis to our low-luminosity sources, the mass as a function of velocity derived from the JCMT data, assuming LTE, an excitation temperature of 20 K, and optically thin emission, also have  $\gamma \sim -1.8$  if we fit a single power law (Fig. 10). However, what is also quite clear is that a single power law is not a good model for the data, and if we were to insist upon fitting power laws, we would need at least two with very different slopes from the  $-1.8$  seen in other objects (see Fig. 10).

We note that in calculating the mass of high-velocity gas in outflows from CO spectra a single excitation temperature and optical depth for the entire line wing is almost always assumed. This was the case for the three sources for which  $\gamma$  was measured by Masson & Chernin (1992). This means that log-log plots of  $dM/dV$  versus  $V$  are directly equivalent to log-log plots of the line profile. Power laws have been fitted to the line wings in a number of other sources, including Orion-KL (Kuiper, Rodríguez Kuiper, & Zuckerman 1978), Cep A, and HL Tau (Rodríguez et al. 1982). The values of  $\gamma$  vary from  $-1.2$  to  $-2.1$  in those objects, and like TMC-1 and TMC-1A, the spectrum of Orion-KL is not well modeled by a single power law. These results suggest that a power law with  $\gamma \sim -1.8$  should not be considered a universal feature of young outflows.

#### 4.5. Comparison with Outflow Models

Considerable observational evidence now exists that jets play an important role in driving outflows (e.g., Bachiller & Cernicharo 1990; Bachiller et al. 1990; Richer, Hills, & Padman 1992). There has been a corresponding theoretical push to explain molecular outflows and optical jets in terms of a unified model, based on the concept of a high-velocity neutral jet which drives the outflow (Stahler 1993; Masson

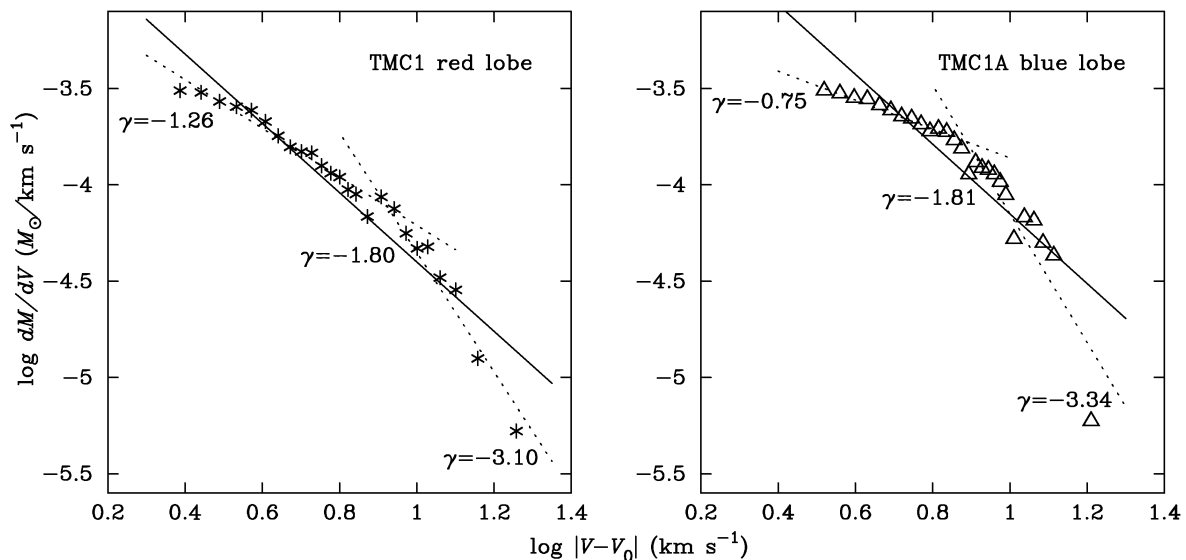


FIG. 10.—Plots of mass as a function of velocity for the red lobe of TMC-1 (left) and the blue lobe of TMC-1A (right).  $V_0$  is the systemic velocity of each source (i.e.,  $5.5 \text{ km s}^{-1}$  for TMC-1, and  $6.4 \text{ km s}^{-1}$  for TMC-1A). A power-law fit to the full data set,  $dM/dV \propto V^\gamma$ , is shown as the solid line in each case. Two-component power-law fits are also displayed as dotted lines.

& Chernin 1993; Raga et al. 1993). We suggest the following properties are common features of young outflows which theoretical models should try to explain: (1) conical outflow lobes close to the star, (2) evacuated outflow cavities, and (3) moderate  $30^{\circ}$ – $45^{\circ}$  opening angles.

The outflow models fall into the general categories of those driven by a radial stellar wind (Shu et al. 1991) and those driven by jets, either through shocks (Masson & Chernin 1993; Raga et al. 1993; Raga & Cabrit 1993) or through turbulent entrainment (Cantó & Raga 1991; Stahler 1994).

In the swept-up outflow proposed by Shu et al. (1991) and analyzed by Masson & Chernin (1992) the outflow is driven by a radial stellar wind into the surrounding medium, and the shape of the outflow is defined by the distribution of the driving pressure and the column density of swept-up material. Shu et al. showed that the swept-up model could result in the elongated outflows commonly observed, but Masson & Chernin argued that for reasonable distributions of the wind and cloud core the swept-up outflow model has problems reproducing plots of mass as a function of velocity. The cavity in this model is filled only with low-density material from the stellar wind. The swept-up wind model naturally reproduces the conical shape, evacuated cavity, and moderate opening angle suggested by observations. However, countering the objections raised by Masson & Chernin (1992) requires a near-spherical wind with a highly flattened density profile near the star to provide the collimation. Although this picture is possible, there is also the less desirable effect that molecular bullets and optical stellar jets then have to be explained by a separate mechanism.

We next consider jet-driven outflow models, in which a highly collimated neutral jet drives the outflow and transfers momentum to the ambient medium through shocks. Masson & Chernin (1993) treat the earliest stages of jet evolution, where momentum is transferred primarily through the leading bow shock, via a high-pressure cocoon of shocked gas which sweeps up ambient material as it expands away from the jet axis. A thin cocoon of swept up gas is identified with the molecular outflow. This class of models produces jets which are too narrow and too young (less than 1000 yr), although they can produce an evacuated outflow cavity (Chernin et al. 1994; Chernin & Masson 1995). A different approach was followed by Raga & Cabrit (1993), who treat the interaction of the bow shock with the ambient medium as a process of turbulent entrainment, leading to a thick cocoon of turbulent ambient material. Raga et al. (1993) propose a model appropriate to the later stages of jet evolution, in which a time-variable jet produces many bow shocks along its length, leading to a turbulent envelope. The latter models can produce conical outflow structure close to the star, although the cone is still too narrow (Raga & Cabrit 1993; Raga et al. 1993). However, the turbulent mixing generates a mostly filled rather than evacuated outflow cavity, contrary to observations.

An alternative to shock acceleration is a situation where the acceleration of molecular gas is achieved through steady state turbulent entrainment of ambient material along the edge of the jet (Cantó & Raga 1991; Stahler 1994). In the analysis presented by Stahler, which assumed the ambient medium to be of uniform density, the outflow would have a conical structure at low velocities, with the highest velocity molecular gas located closest to the jet axis. However, the model produces a filled rather than evacuated outflow

cavity. In addition, the model has difficulty reconciling observations of stellar jets with those of molecular outflows (see Raga 1994).

Of our three constraints, jet models seem able to explain the conical shape near the star given a density gradient (Raga & Cabrit 1993; Raga et al. 1993), while the evacuated cavity can be produced in the momentum-conserving models which minimize turbulent entrainment (Chernin & Masson 1995). The most severe observational constraint is the moderate  $30^{\circ}$ – $45^{\circ}$  opening angle, which is very difficult for jet models to reproduce. Masson & Chernin (1993) proposed a wandering jet to provide larger opening angles, a picture later elaborated as the wandering dentist drill (Chernin & Masson 1995). However, this scenario seems likely to produce messy outflow structures, rather than the symmetric cones that are observed around young sources. Recent models (Biro, Raga, & Cantó 1995) present an alternative implementation of the wandering jet hypothesis. Their two-dimensional numerical simulation leads to a sinuous jet, with a different bow shock apparent at every S-shaped turn, very unlike the structure of observed stellar jets. Further numerical modeling will be needed to determine whether jet models can reproduce the moderate opening angles observed toward young protostars.

#### 4.6. *Apparent Acceleration along the Outflow Axis*

The apparent acceleration of molecular material away from the exciting star has been observed in a number of sources (e.g., NGC 2071: Snell et al. 1984; L1551: Moriarty-Schieven & Snell 1988; Mon R2: Meyers-Rice & Lada 1991) but never before on the small scales we see for TMC-1 and TMC-1A. A number of models seek to explain the phenomenon. Meyers-Rice & Lada suggest that “velocity-sorting” of clumps entrained by a wind or jet would result in the fastest moving material being located at the largest distance from the source, giving rise to the observed velocity distribution.

The jet-entrainment model provides an alternative explanation (Stahler 1994), where the apparent acceleration is a column density effect. High velocities exist at all radii, but the jet will have entrained more material at larger distances from the source, bringing its emission into the range of detectability. This requires the highest velocity material to be located along the jet axis, and the outflow lobes to be filled with molecular gas. While the highest velocity emission is often also observed to be the most collimated (e.g., Richer et al. 1992), this does not necessarily indicate that the outflow has to be filled with molecular material; in projection, a hollow cone will have its highest radial velocities apparently more collimated than lower velocity gas.

Although the maximum velocities observed in TMC-1 and TMC-1A are relatively low ( $\sim 30 \text{ km s}^{-1}$  for an inclination angle of  $60^{\circ}$ ) they are close to the limit at which molecules would be destroyed if the acceleration mechanism is a nonmagnetic shock ( $30$ – $50 \text{ km s}^{-1}$ : McKee & Hollenbach 1980). In this case trans-sonic or subsonic entrainment either by a wandering jet or by the bow shock may be essential in accelerating the molecular gas without causing excessive heating, so that the molecules are not destroyed.

## 5. CONCLUSIONS

High-resolution imaging of the compact outflows associated with the sources TMC-1 and TMC-1A in CO(1–0) shows that the outflows are conical down to scales of 1000

AU, with the apex of the cone close to the position of the millimeter continuum source in each case. The dynamics of the flows, determined from CO(2–1) data, indicate that they are low-luminosity versions of the more energetic outflows. Both the momentum flux and the mechanical luminosity of the flows follow the correlation between these quantities and the source bolometric luminosity determined by Cabrit & Bertout (1992). A comparison of the  $J = 2-1$  transition with the 1–0 gives a lower limit to the excitation temperature in the line wing of 20 K, which is somewhat higher than the average temperature of molecular gas in the Taurus cloud ( $\sim 10$  K). This suggests that the high-velocity gas has been heated locally, perhaps by the passage of a shock.

The conical structure of the outflows is also apparent in near-infrared  $H$  and  $K$  images, which show extended near-infrared emission coincident with the high-velocity CO. Quantitative scattering models (Whitney & Hartmann 1993) demonstrate that the lobes must be evacuated to explain the large spatial extent and structure of the extended near-infrared emission. In addition, the CO(2–1) position-velocity diagrams show features corresponding to the front and back of a limb-brightened shell. These results for TMC-1 and TMC-1A bolster the results of Kenyon et al. (1993b), which suggest that most embedded sources have evacuated outflow cavities.

By comparing our P-V diagrams and line profiles with the outflow models of Cabrit & Bertout (1986, 1990) we constrain the inclination of both flows to the line of sight to be  $i \lesssim 70^\circ$ . The inclination can be further limited by comparing the extended infrared reflection nebulosity with the Monte Carlo scattering models of Whitney & Hartmann (1993), which suggest  $i \gtrsim 40^\circ$ . This technique of combining near-infrared and CO observations can be used to determine inclinations toward other embedded infrared sources, especially those showing conical structure. The deprojected opening angles of the conical flows in TMC-1 and TMC-1A

are then  $30^\circ$ – $40^\circ$ , similar to those observed in the class 0 sources VLA 1623, B335, and L1448-C (André et al. 1990; Chandler & Sargent 1993; Bachiller et al. 1995).

Taken together, the data suggest that the following properties are important for theoretical outflow models to explain, namely, that young outflows have: (1) conical outflow lobes close to the star, (2) evacuated outflow cavities, and (3) moderate  $30^\circ$ – $45^\circ$  opening angles. None of the current outflow models satisfactorily explains the results. As found by Masson & Chernin (1992), outflows driven by radial stellar winds cannot reproduce the line profile without unreasonably highly flattened cloud cores. Steady state turbulent jet models (Cantó & Raga 1991; Stahler 1994), where molecular gas is accelerated through turbulent entrainment along the edges of a collimated jet, produce a conical shape but a filled rather than evacuated cavity. Jet-driven bow shocks, in which a bow shock accelerates ambient material, in some cases can produce conical evacuated outflow cavities but fail to reproduce the large opening angles and give ages which are too young (Masson & Chernin 1993; Raga & Cabrit 1993; Raga et al. 1993; Chernin & Masson 1995). Extending the jet model to include a wandering jet provides a possible way to provide large opening angles (Chernin & Masson 1995; Biro et al. 1995) but this possibility remains to be demonstrated.

Part of this work was carried out while C. J. C. was a Jansky Fellow at the National Radio Astronomy Observatory, Socorro, New Mexico. M. B. acknowledges financial support from the US National Science Foundation's Faculty Early Career Development Program, grant AST 95-01788. This research was carried out in part at the Jet Propulsion Laboratory, California Institute of Technology, under a contract with the National Aeronautics and Space Administration. Research at the Owens Valley Radio Observatory is supported by NSF grant AST 93-14079.

#### REFERENCES

- André, P., Martín-Pintado, J., Despois, D., & Montmerle, T. 1990, *A&A*, 236, 180
- André, P., Ward-Thompson, D., & Barsony, M. 1993, *ApJ*, 406, 122
- Bachiller, R., & Cernicharo, J. 1990, *A&A*, 239, 276
- Bachiller, R., Cernicharo, J., Martín-Pintado, J., Tafalla, M., & Lazareff, B. 1990, *A&A*, 231, 174
- Bachiller, R., Guilloteau, S., Dutrey, A., Planesas, P., & Martín-Pintado, J. 1995, *A&A*, 299, 857
- Bally, J., & Lada, C. J. 1983, *ApJ*, 265, 824
- Biro, S., Raga, A. C., & Cantó, J. 1995, *MNRAS*, 275, 557
- Bontemps, S., André, P., Terebey, S., & Cabrit, S. 1996, *A&A*, in press
- Cabrit, S., & Bertout, C. 1986, *ApJ*, 307, 313
- . 1990, *ApJ*, 348, 530
- . 1992, *A&A*, 261, 274
- Cantó, J., & Raga, A. C. 1991, *ApJ*, 372, 646
- Chandler, C. J., & Sargent, A. I. 1993, *ApJ*, 414, L29
- Chernin, L. M., & Masson, C. R. 1995, 455, 182
- Chernin, L., Masson, C., Gouveia Dal Pino, E. M., & Benz, W. 1994, 426, 204
- Edwards, S., Ray, T., & Mundt, R. 1993, in *Protostars and Planets III*, ed. E. H. Levy & J. I. Lunine (Tucson: Univ. Arizona Press), 567
- Elias, J. H., Frogel, J. A., Matthews, K., & Neugebauer, G. 1982, *AJ*, 87, 1029
- Heyer, M. H., Ladd, E. F., Myers, P. C., & Campbell, B. 1990, *AJ*, 99, 1585
- Heyer, M. H., Snell, R. L., Goldsmith, P. F., & Myers, P. C. 1987, *ApJ*, 321, 370
- Hirano, N., Kameya, O., Nakayama, M., & Takakubo, K. 1988, *ApJ*, 327, L69
- Kenyon, S. J., Calvet, N., & Hartmann, L. 1993a, *ApJ*, 414, 676
- Kenyon, S. J., Whitney, B. A., Gomez, M., & Hartmann, L. 1993b, *ApJ*, 414, 773
- Kuiper, T. B. H., Rodriguez Kuiper, E. N., & Zuckerman, B. 1978, *ApJ*, 219, 129
- Lada, C. J. 1985, *ARA&A*, 23, 267
- Masson, C. R., & Chernin, L. M. 1992, *ApJ*, 387, L47
- . 1993, *ApJ*, 414, 230
- McKee, C. F., & Hollenbach, D. J. 1980, *ARA&A*, 18, 219
- Meyers-Rice, B. A., & Lada, C. J. 1991, *ApJ*, 368, 445
- Moriarty-Schieven, G. H., & Snell, R. L. 1988, *ApJ*, 332, 364
- Murphy, D. C., & Myers, P. C. 1985, *ApJ*, 298, 818
- Myers, P. C., Fuller, G. A., Mathieu, R. D., Beichman, C. A., Benson, P. J., Schild, R. E., & Emerson, J. P. 1987, *ApJ*, 319, 340
- Parker, N. D., Padman, R., & Scott, P. F. 1991, *MNRAS*, 252, 442
- Raga, A. 1994, *Ap&SS*, 216, 105
- Raga, A., & Cabrit, S. 1993, *A&A*, 278, 267
- Raga, A. C., Cantó, J., Calvet, N., Rodríguez, L. F., & Torrelles, J. 1993, *A&A*, 276, 539
- Richer, J. S., Hills, R. E., & Padman, R. 1992, *MNRAS*, 254, 525
- Rieke, G. H., & Lebofsky, M. J. 1985, *ApJ*, 288, 618
- Rodríguez, L. F., Carral, P., Moran, J. M., & Ho, P. T. P. 1982, *ApJ*, 260, 635
- Shu, F. H., Ruden, S. P., Lada, C. J., & Lizano, S. 1991, *ApJ*, 370, L31
- Snell, R. L., Scoville, N. Z., Sanders, D. B., & Erickson, N. R. 1984, *ApJ*, 284, 176
- Stahler, S. W. 1993, in *Astrophysical Jets*, ed. D. Burgarella, M. Livio, & C. P. O'Dea (Cambridge: Cambridge Univ. Press) 183
- . 1994, *ApJ*, 422, 616
- Tamura, M., Gatley, I., Waller, W., & Werner, M. W. 1991, *ApJ*, 374, L25
- Terebey, S., Beichman, C. A., Gautier, T. N., & Hester, J. J. 1990, *ApJ*, 362, L63
- Terebey, S., Chandler, C. J., & André, P. 1993, *ApJ*, 414, 759
- Terebey, S., Vogel, S. N., & Myers, P. C. 1989, *ApJ*, 340, 472
- . 1992, *ApJ*, 390, 181
- Whitney, B. A., & Hartmann, L. 1993, *ApJ*, 402, 605